Analysis of Low-Frequency Oscillation in Electric Railways Based on Small-Signal Modeling of Vehicle-Grid System in *dq* Frame

Hui Wang, Wu Mingli, and Juanjuan Sun

***Abstract*—The line-side converter, which can represent an ac–dc–ac drive electric vehicle when analyzing the low-frequency oscillation in electric railways, is modeled in *dq* frame with the proposed single-phase *dq*-decomposition method. With this model, an underdamped mechanism of the vehicle-grid interaction is confirmed. Besides, a low-frequency stability prediction approach is presented, based on the dominant-pole analysis and verified by the simulation and the testing result. The proposed modeling method and prediction approach benefit in three aspects: It is more convenient to rebuild the model with a change of either the line-side converter controller or the system condition, much quicker to predict the low-frequency instability and more explicit to guide the modification of the controller software to damp the low-frequency oscillations.**

***Index Terms*—Dominant pole, *dq*-frame modeling, electric railway, line-side converter, low-frequency oscillation (LFO).**

I. Introduction

RECENT years, with more and more ac–dc–ac drive electric locomotives and EMUs (hereinafter, referred to as electric rail vehicles) being put into operation, the low-frequency oscillation (LFO) events have occurred worldwide in different kinds of traction power supply systems. According to the published literatures known by the authors, the LFO first happened in a Norwegian railway, where the rotary converters are adopted in traction substations [1]. Then, this phenomenon occurred successively in Germany, USA, Switzerland, France, and China. Among them, the LFOs in France and China are called as a "depot problem" because they usually happened when a large number of vehicles were at standstill in a railway depot or station with only the auxiliary load powered by the dc-link of traction converters. The LFOs occurred in China are summarized in Table I and [2]–[4]. This paper will mainly focus on this type of LFO based on the field measurement conducted for CRH_5 EMU in Chinese railway. It has been demonstrated that the LFO may trigger the protection logic of line-side converters (LSCs) to shut down the vehicle's traction system and, hence, normally result in a severe service delay.

TABLE I
LFO Cases in China Electric Railways

Case No.	Vehicle type	Oscillation frequency f_l /Hz	Occurrence time
1	HX_D 1	3–4	2008.01
2	CRH_1	5	2010.01
3	CRH_5	5	2010.09
4	HX_D 2B	5	2011.06
5	HX_D 3B	6–7	2011.11

In order to understand the LFO, which is in fact a complicated vehicle-grid interaction problem, some dedicated testing, modeling, and simulating works are needed to explore its mechanism and, then, to propose appropriate damping methods. Unfortunately, up to now, few studies have been conducted to explain this phenomenon. A simulation model has been built to illustrate the impact of the long contact line and the vehicle number on the LFO [5]. The instability is attributed to a "negative impedance mechanism" by modeling the rotary converter substation and the vehicle in the frequency domain [6]. Then, a detailed instantaneous value modeling is presented to investigate the mechanism of LFO with the eigenvalues analysis [7]. To improve the low-frequency stability, a multivariable control strategy has been adopted [8]. However, all these studies have their own limits. First, it is not sufficient to reveal the mechanism of LFO in an electric railway system with the simulation alone. Second, the rotary converter, which contributes significantly to the instability, has not been applied in the "depot problem" cases. Third, although the eigenvalue analysis can determine the risk of low-frequency instability, it will take a long time to rebuild the entire system differential equations even only a single LSC controller parameter changes. Finally, without an unambiguous understanding of the LFO mechanism, the damping control strategy is hard to be widely applied to different types of vehicles.

In order to reveal the vehicle-grid interaction in a more systematic way, it is necessary to build an analytical vehicle (represented by LSCs) model. A small-signal frequency-domain modeling method has been considered for linearizing the LSC, since the power electronic devices are nonlinear due to the switches and the controllers, and needed to be linearized around the steady-state operation point [9]. It has already been widely used to solve the source-load interaction problems in other power electronic applications, first for the interconnected dc–dc

Manuscript received September 21, 2014; revised November 8, 2014; accepted December 29, 2014. Date of publication January 6, 2015; date of current version April 15, 2015. This work was supported by the Fundamental Research for the Central Universities of China under Grant 2012JBZ006. Recommended for publication by Associate Editor D. Vinnikov. *(Corresponding author: Wu Mingli).*

H. Wang and W. Mingli are with the School of Electrical Engineering, Beijing Jiaotong University, Beijing 100044, China (e-mail: 09117353@bjtu.edu.cn; mlwu@bjtu.edu.cn).

J. Sun is with the School of Mechanical, Electronic, and Control Engineering, Beijing Jiaotong University, Beijing 100044, China (e-mail: jjsun@bjtu.edu.cn).

Color versions of one or more of the figures in this paper are available online at http://ieeexplore.ieee.org.

Digital Object Identifier 10.1109/TPEL.2015.2388796

converters [10], [11], then for the three-phase ac system with the *dq* transformation, which can transform an ac operation point to a dc one [12]–[15]. The small-signal modeling of power electronic devices and the impedance-based system stability analysis have the essence of dividing the interconnected system to a source subsystem and a load subsystem so that the rebuilt of the whole system model can be avoided when there are some changes in one load or the number of them [16], [17]. So this modeling method is a useful guidance when analyzing the vehicle-grid interaction.

However, for a single-phase ac system, the modeling difficulty is how to linearize the power converter operating in a periodic sinusoidal trajectory. To solve this problem, various methods have been resorted in the literatures, such as the reduced-order method for the single-phase PFC and the grid-connected inverters [18], [19], the phasor method for the distributed generation resources [20], the harmonic linearization method for the line-frequency rectifier [21], [22], and the harmonic-domain matrix method for the EMU LSC [23]. These methods either focus on the high-frequency performance of the system or target on the power converters whose structure and controller strategy are quite different from the LSC of an electric rail vehicle, so that they cannot be directly applied in the LFO problem.

The *dq*-frame control is adopted for the LSCs of CRH_5 EMU. Considering the important influence of a converter controller on its dynamic performance, it is reasonable to model the representative LSC in *dq* synchronous coordination. The *dq*-frame model of an EMU LSC has first been brought up as a concept in [24] and, then, its numerical value has been calculated out through experiments in [25] and [26]. However, there is no paper documenting an analytical model of a single-phase LSC in *dq* frame since it will bring noticeable error due to the nonexistence of the β-axis signal as in the three-phase system and, hence, be infeasible in a wide frequency range. In fact, because the small-signal variations of the voltage and current occur in a very narrow sideband frequency range around the fundamental frequency in the LFO, this error can be modeled as a linear function and, then, an analytical small-signal frequency-domain model of LSC could still be built in *dq* frame.

The rest of this paper is organized as follows. In Section II, the fundamental theory for a single-phase ac system modeling that focuses on the LFO problem is introduced by the analysis of the measured data obtained from an "oscillating" vehicle. In Section III, the LSC is modeled as an admittance matrix including its main circuit and controller. Then, this analytic model is verified by comparison with time-domain simulation results. In Section IV, the resultant vehicle-grid system model is derived out. In Section V, the mechanism of LFO is obtained by analyzing the dominant poles of the vehicle-grid system and some factors that can affect the LFO are discussed. Finally, Section VI concludes this paper.

II. Fundamental Theory

A. Unsymmetrical Sideband Harmonics in LFO

According to the observation of continuous records of the line voltage and vehicle current waveforms during the LFOs, it is found that the oscillation may finally develop into three possible states: Decaying to disappear, maintaining stable, and enlarging till to trigger the LSC protection and, then, disappearing.

In the practical LFO cases, when the vehicle-grid system is in the stable oscillation state, the line voltage and vehicle current can be decomposed into three main components (the high-frequency harmonic components are not included here due to their negligible influence on the LFO)

$$\begin{aligned} x(t) = {} & X_0\cos(2\pi f_0 t+\delta_0) \\ & + X_+\cos\left[2\pi f_+ t+\delta_+\right] \\ & + X_-\cos\left[2\pi f_- t+\delta_-\right] \\ f_+ = {} & f_0+f_l, f_- = f_0-f_l \end{aligned} \tag{1}$$

where x represents the line voltage or the vehicle current. X_0 and δ_0 are the amplitude and initial phase of the fundamental frequency component, and similarly X_+, X_-, δ_+, δ_- are those of sideband harmonics. f_0 and f_l are the fundamental frequency and the oscillation frequency, respectively. The reported range of f_l is 10–30% of the fundamental frequency in [6]. However, in the "depot problems" of Chinese railway, its scope is found to be 6–14% of the fundamental frequency (i.e., 3 to 7 Hz as shown in Table I). It should be noted that there actually does not exist an f_l component in the oscillating signals. The oscillating waveform can be more appropriately described as an unsymmetrical amplitude modulation since X_+ and X_- are normally unequal. As an example, Fig. 1 gives the measured oscillating line voltage and vehicle current waveforms and corresponding harmonic spectra in a LFO event caused by CRH_5.

B. Dq Decomposition of Single-Phase AC Signal

By proper trigonometric calculations, (1) can be rewritten as

$$\begin{aligned} x(t) = {} & \left[x_{d0}+X_d\cos(\omega_l t+\theta_d)\right]\cos(\omega_0 t) \\ & -\left[x_{q0}+X_q\cos(\omega_l t+\theta_q)\right]\sin(\omega_0 t) \end{aligned} \tag{2}$$

where

$$\begin{aligned} & \omega_0 = 2\pi f_0 t, \omega_l = 2\pi f_l t \\ & x_{d0} = X_0\cos(\delta_0), x_{q0} = X_0\sin(\delta_0) \\ & X_d = \\ & \sqrt{[X_+\cos(\delta_+)+X_-\cos(\delta_-)]^2+[X_+\sin(\delta_+)-X_-\sin(\delta_-)]^2} \\ & \theta_d = \arctan\left[\frac{X_+\sin(\delta_+)-X_-\sin(\delta_-)}{X_+\cos(\delta_+)+X_-\cos(\delta_-)}\right] \\ & X_q = \\ & \sqrt{[X_-\cos(\delta_-)-X_+\cos(\delta_+)]^2+[X_+\sin(\delta_+)+X_-\sin(\delta_-)]^2} \\ & \theta_q = \arctan\left[\frac{X_-\cos(\delta_-)-X_+\cos(\delta_+)}{X_+\sin(\delta_+)+X_-\sin(\delta_-)}\right] \end{aligned} \tag{3}$$

By carefully observing (2), it can be found that the signal x conforms, in fact, to the definition of the inverse Park transformation, which transforms a variable from the *dq*-rotating frame to the $\alpha\beta$-stationary frame for a three-phase system. Referring

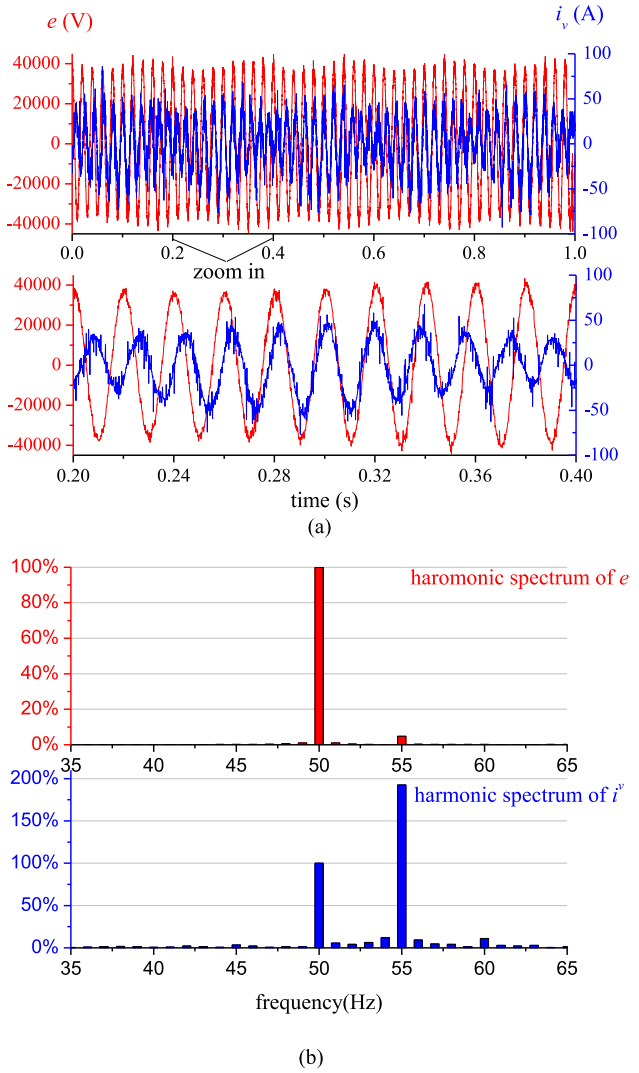

Fig. 1. (a) Measured oscillating waveforms. (b) Harmonic spectra of measured oscillating waveforms.

to this concept, the *dq*-frame expression of x can be defined as

$$\begin{aligned} x_d &= x_{d0} + X_d \cos(\omega_l t + \theta_d) = x_{d0} + \Delta x_d \\ x_q &= x_{q0} + X_q \cos(\omega_l t + \theta_q) = x_{q0} + \Delta x_q \end{aligned} \tag{4}$$

where x_{d0}, x_{q0} can be considered as the d-axis and q-axis steady-state values and Δx_d, Δx_q are the small-signal variations. It has been shown in (4) that the fundamental frequency component has been transformed into a dc component in *dq* frame and the f_+/f_- sideband harmonics have been transformed into a sinusoidal variation at frequency f_l in *dq* frame. As this *dq* frame has the constant rotating frequency f_0, it is defined as the grid *dq* frame for the purpose to distinguish from another *dq* frame that will be mentioned in the following analysis.

C. Small-Signal Analysis of Vehicle-Grid System

An LSC shows an admittance characteristic since its voltage disturbance can be treated as input and its current variation as output. As a result, with two inputs and two outputs, the

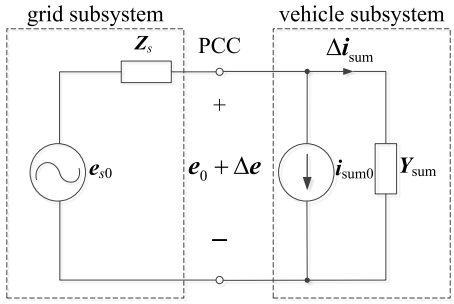

Fig. 2. Small-signal vehicle-grid system.

small-signal model of an LSC in *dq* frame can be described by an input admittance matrix

$$\boldsymbol{Y} = \frac{\Delta \boldsymbol{i}}{\Delta \boldsymbol{e}}, \quad \Delta \boldsymbol{i} = [\Delta i_d \quad \Delta i_q]^T, \quad \Delta \boldsymbol{e} = [\Delta e_d \quad \Delta e_q]^T \tag{5}$$

where the bold and italic letter in lowercase denotes a vector variable in the grid *dq* frame. To verify the linearity of $\boldsymbol{Y}$, a time-domain simulation of LSC has been conducted in advance using MATLAB/Simulink. Then, the numeric values of $\boldsymbol{Y}$ at different frequencies can be obtained through a low-frequency sweep experiment, which will be introduced in Section III. Therefore, the elements of $\boldsymbol{Y}$ can be calculated as follows:

$$\begin{aligned} Y_{dd}(j\omega_l) &= \frac{|\Delta i_d(j\omega_l)|}{|\Delta e_d(j\omega_l)|} \angle [\angle \Delta i_d(j\omega_l) - \angle \Delta e_d(j\omega_l)] \\ Y_{qq}(j\omega_l) &= \frac{|\Delta i_q(j\omega_l)|}{|\Delta e_q(j\omega_l)|} \angle [\angle \Delta i_q(j\omega_l) - \angle \Delta e_q(j\omega_l)] \\ Y_{dq}(j\omega_l) &= \frac{|\Delta i_d(j\omega_l)|}{|\Delta e_q(j\omega_l)|} \angle [\angle \Delta i_d(j\omega_l) - \angle \Delta e_q(j\omega_l)] \\ Y_{qd}(j\omega_l) &= \frac{|\Delta i_q(j\omega_l)|}{|\Delta e_d(j\omega_l)|} \angle [\angle \Delta i_q(j\omega_l) - \angle \Delta e_d(j\omega_l)] \end{aligned} \tag{6}$$

The calculation result indicates that the values of $\boldsymbol{Y}$ at a certain frequency keep unchanged regardless how the input voltage disturbance changes. This, in fact, guarantees the feasibility of the linear small-signal analysis.

As for the traction power feeding grid, it can be modeled as a Thevenin equivalent circuit due to the narrow interesting frequency range (f_- to f_+ in stationary frame), and is therefore linear [7], [27]. Then the small-signal vehicle-grid system in *dq* frame can be depicted as Fig. 2. In Fig. 2, $\boldsymbol{e}_{s0}$, $\boldsymbol{e}_0$, and $\boldsymbol{i}_{\mathrm{sum}0}$ denotes the steady-state vectors of the source voltage, point of common coupling (PCC) voltage (i.e., line voltage), and the sum current of m vehicles in the grid *dq* frame. $\Delta \boldsymbol{e}$ and $\Delta \boldsymbol{i}_{\mathrm{sum}}$ are the small-signal vectors of PCC voltage and the sum current of m vehicles in the grid *dq* frame. $\boldsymbol{Y}_{\mathrm{sum}}$ is the total input admittance matrix of m vehicles and $\boldsymbol{Z}_s$ is the grid impedance matrix. They will be derived in Sections III and IV, respectively.

III. Model of CRH_5 LSC

The available information on the main circuit and the controller of the LSC of the CRH_5 EMU is relatively complete.

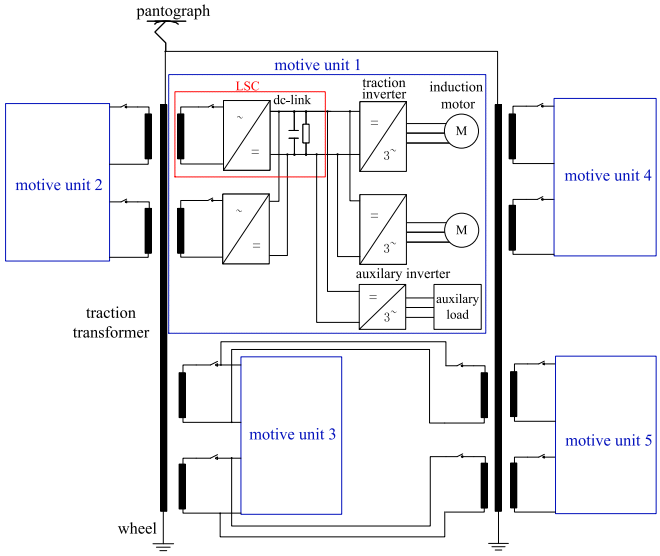

Fig. 3. Structure of CRH_5 EMU.

Some controller modules, which are not introduced in detail in the manufacturer documents, refer to [7]. The controller parameters are reasonably set according to the controller tuning principle [28]. With these knowledge, the CRH_5 LSC can be divided into several parts according to its main circuit and controller structure and each part can be linearized and modeled in the grid *dq* frame. Then, the small-signal *dq*-frame model of a CRH_5 LSC will be obtained by connecting the models of these parts together.

A. Main Circuit and Controller

The CRH_5 EMU consists of five motive units with the same structure. Among them, three units are powered by one traction transformer and two by the other as shown in Fig. 3. Each unit has two LSCs sharing one common dc-link that supplies two three-phase traction inverters and one auxiliary converter. Each traction inverter powers one induction motor. The equal power-sharing strategy control is adopted for these two LSCs in one motive unit, which means their ac input currents are same [29]. Therefore, two paralleled LSCs can be modeled separately since their circuits and controllers are identical. With this assumption, one CRH_5 will consist of ten LSCs (i.e., $i_v = 10i$). Because the LFO usually happened in the light-load condition when only auxiliary converters were working [2]–[4], [27], the load of the dc-link is simplified as a constant dc current to represent the auxiliary power consumption.

The LSC controller of CRH_5 EMU is designed in *dq* frame. The controller structure includes an ac voltage synchronization system (VSS) and an ac current synchronization system (CSS), an ac current controller (ACC), and a dc voltage controller (DVC). The main circuit and controller of the LSC are described in Fig. 4. In Fig. 4, e_α is the voltage from the pantograph to the wheel, where the subscript α is added in order to distinguish from the orthogonal β-axis variable. i_α is the LSC current. v_α is the ac-side voltage of the converter bridge. $v_{\rm dc}$ is the dc-link voltage, while $i_{\rm dc}$ is the output current of

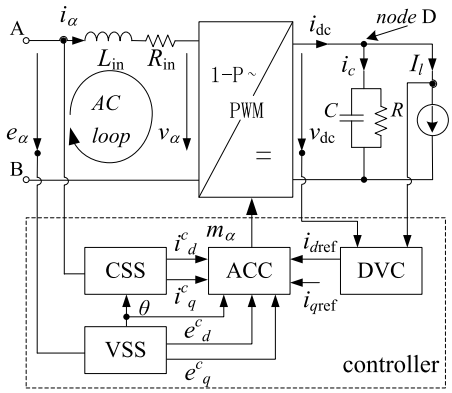

Fig. 4. Line-side converter circuit and its controller.

converter bridge. i_c is the total current that flows through the dc-link capacitor *C* and the paralleled resistance *R*. I_l is the dc load current. $L_{\rm in}$ and $R_{\rm in}$ are the equivalent leakage inductance and resistance of the traction transformer.

In order to make this study applicable to different types of vehicles, all the variables and circuit parameters in the following analyses are expressed in per unit value and the controller parameters are also tuned in per unit system. The subscript p.u. will be omitted for convenience. These values are all provided in Appendix.

B. Synchronization System

The function of VSS is to generate the controller synchronous angle θ, which is used for the Park and inverse Park transformation in controller modules, and to transform e_α to $\boldsymbol{e}^c = [e^c_d \quad e^c_q]^T$. The superscript *c* denotes a variable generated in the LSC controller and a bold italic letter with superscript *c* denotes a controller *dq*-frame vector variable. The angle θ equals to θ_0 in the steady state and will have a small variation $\Delta\theta = \theta - \theta_0$ when the LSC presents a deviation from its steady state. The CSS utilizes the angle θ directly for the Park transformation to generate $\boldsymbol{i}^c = [i^c_d \quad i^c_q]^T$.

The objective of the following analysis is to find the relationship between $\Delta\boldsymbol{e}^c$, $\Delta\boldsymbol{i}^c$ and $\Delta\boldsymbol{e}$, $\Delta\boldsymbol{i}$ when the LSC has a dynamic behavior around a certain steady-state operation point.

1) Voltage Synchronization System: The VSS shown in Fig. 5 consists of a PLL, a second-order generalized integrator (SOGI), and a Park transformation module. The SOGI is applied to generate a β-axis signal and to filter the input [7]. According to Fig. 5, e^c_α and e^c_β can be expressed as

$$e^c_\alpha = \frac{K_{e\rm SOGI}\omega_0 s}{s^2 + K_{e\rm SOGI}\omega_0 s + \omega_0^2} e_\alpha = H_e(s) e_\alpha \tag{7}$$

$$e^c_\beta = H_e(s)\frac{\omega_0}{s} e_\alpha = H_e(s) e_\beta \tag{8}$$

where e_β is defined as a $1/(4f_0)$ delay signal of e_α. The signal e_β also conforms to the definition of the fictional β-axis signal that is widely used in the traditional *dq*-decomposition technique of a single-phase ac signal [30]–[32]. Recall that e_α has the form of (1) in the LFO situation, e_α and e_β can then be expressed by their definition and reorganized as

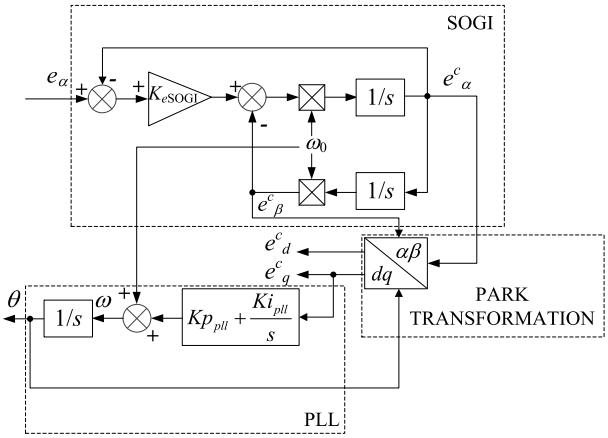

Fig. 5. Structure of VSS.

$$\begin{aligned} e_\alpha &= E_0\cos(\omega_0 t+\delta_e) \\ &\quad + E_+\cos(\omega_+ t+\delta_{e+}) + E_-\cos(\omega_- t+\delta_{e-}) \qquad (9) \\ e_\beta &= E_0\sin(\omega_0 t+\delta_e) \\ &\quad + \frac{f_0}{f_+}E_+\sin(\omega_+ t+\delta_{e+}) + \frac{f_0}{f_-}E_-\sin(\omega_- t+\delta_{e-}) \qquad (10) \end{aligned}$$

To obtain the *dq* frame vector $\boldsymbol{e}$ with the form of (4), the Park transformation is applied to the stationary-frame vector $\mathbf{e}=[e_\alpha \quad e_\beta]^T$, where a bold letter denotes a stationary-frame vector. Instead of $\boldsymbol{e}$, the transformation result is $\boldsymbol{e}'$ in the LFO state, which can be expressed as

$$\begin{aligned} \boldsymbol{e}' &= \begin{bmatrix}\cos(\theta_0) & \sin(\theta_0)\\ -\sin(\theta_0) & \cos(\theta_0)\end{bmatrix}\mathbf{e} = \boldsymbol{P}_{\theta_0}\mathbf{e} \\ &= \underbrace{\begin{bmatrix}e_{d0}\\ e_{q0}\end{bmatrix}}_{\boldsymbol{e}_0} + \underbrace{\begin{bmatrix}\Delta e_d\\ \Delta e_q\end{bmatrix}}_{\Delta\boldsymbol{e}} + \underbrace{\begin{bmatrix}e_{d\mathrm{err}}\\ e_{q\mathrm{err}}\end{bmatrix}}_{\boldsymbol{e}_{\mathrm{err}}} \\ &= \boldsymbol{e}+\boldsymbol{e}_{\mathrm{err}} = \boldsymbol{e}_0+\Delta\boldsymbol{e}' \qquad (11) \end{aligned}$$

In (11), $\boldsymbol{e}_0$ and $\Delta\boldsymbol{e}$ can be obtained by (4) and $\boldsymbol{P}_{\theta_0}$ is the Park transformation matrix with the synchronous angle θ_0. From (11) and (12) shown at the bottom of the page, it's readily to understand that: 1) If the LSC is in the steady state, there is neither a variation component $\Delta\boldsymbol{e}$ nor an error component $\boldsymbol{e}_{\mathrm{err}}$ when applying the Park transformation on $\mathbf{e}$. 2) If the LSC is in the LFO state, there will be an error between the Park transformation result $\boldsymbol{e}'$ and the grid *dq*-frame vector $\boldsymbol{e}$ defined in (4). 3) The error component $\boldsymbol{e}_{\mathrm{err}}$ is nonlinear. In fact, $\boldsymbol{e}_{\mathrm{err}}$ is the main obstacle when attempting to model a single-phase ac system in *dq* frame.

With the knowledge that f_l is normally under 15% of the fundamental frequency, f_l/f_+ and f_l/f_- can be approximately substituted by f_l/f_0, which only brings a maximal inaccuracy of 2.65%. Then $\boldsymbol{e}_{\mathrm{err}}$ can be further reformulated as

$$\begin{bmatrix}e_{d\mathrm{err}}\\ e_{q\mathrm{err}}\end{bmatrix} = \begin{bmatrix}\frac{f_l}{2f_0}E_q cos\left(\omega_l t+\theta_q-\frac{\pi}{2}\right)\\ \frac{f_l}{2f_0}E_d cos\left(\omega_l t+\theta_q+\frac{\pi}{2}\right)\end{bmatrix} \qquad (13)$$

It can be readily discovered that

$$\begin{bmatrix}|e_{d\mathrm{err}}(j\omega_l)|\\ |e_{q\mathrm{err}}(j\omega_l)|\end{bmatrix} = \begin{bmatrix}\left|\frac{\omega_l}{2\omega_0}\right|\cdot\left|\frac{d\Delta e_q}{dt}\right|\\ \left|\frac{\omega_l}{2\omega_0}\right|\cdot\left|\frac{d\Delta e_d}{dt}\right|\end{bmatrix} \qquad (14)$$

$$\begin{bmatrix}\angle e_{d\mathrm{err}}(j\omega_l)\\ \angle e_{q\mathrm{err}}(j\omega_l)\end{bmatrix} = \begin{bmatrix}-\angle\frac{d\Delta e_q}{dt}\\ \angle\frac{d\Delta e_d}{dt}\end{bmatrix} \qquad (15)$$

through the comparison of (4) with (13). So, in the frequency domain, $\boldsymbol{e}_{\mathrm{err}}$ can be linearized and the relation between $\Delta\boldsymbol{e}'$ and $\Delta\boldsymbol{e}$ could be derived as

$$\Delta\boldsymbol{e}' = \begin{bmatrix}1 & -\frac{s}{2\omega_0}\\ \frac{s}{2\omega_0} & 1\end{bmatrix}\Delta\boldsymbol{e} = \boldsymbol{T}\Delta\boldsymbol{e} \qquad (16)$$

Hence, the main modeling problem is properly solved by introducing an adjusting matrix $\boldsymbol{T}$.

Then, according to Fig. 5, the output of VSS $\boldsymbol{e}^c$ can be calculated as

$$\boldsymbol{e}^c = \boldsymbol{P}_\theta\boldsymbol{H}_e\mathbf{e} \qquad (17)$$

where $\boldsymbol{H}_e$ is a diagonal matrix with diagonal elements $H_e(s)$. As the Park and inverse Park transformation can be applied to a steady-state component and a small-signal variation independently [cf., (11)], $\boldsymbol{e}^c$ can also be expressed as

$$\begin{aligned} \boldsymbol{e}^c &= \boldsymbol{P}_\theta\boldsymbol{H}_e\boldsymbol{P}_{\theta_0}^{-1}(\boldsymbol{e}_0+\boldsymbol{T}\Delta\boldsymbol{e}) \\ &\approx \boldsymbol{P}_{\Delta\theta}(\boldsymbol{P}_{\theta_0}\boldsymbol{H}_e\boldsymbol{P}_{\theta_0}^{-1})(\boldsymbol{e}_0+\boldsymbol{T}\Delta\boldsymbol{e}) \\ &\approx \boldsymbol{P}_{\Delta\theta}\boldsymbol{H}_{edq}(\boldsymbol{e}_0+\boldsymbol{T}\Delta\boldsymbol{e}) \qquad (18) \end{aligned}$$

where $\boldsymbol{P}_{\theta_0}^{-1}$ is the inverse Park transformation matrix. $\boldsymbol{P}_{\Delta\theta}$ can be approximately expressed as

$$\boldsymbol{P}_{\Delta\theta} = \begin{bmatrix}1 & \Delta\theta\\ -\Delta\theta & 1\end{bmatrix} \qquad (19)$$

as long as $\Delta\theta$ is small enough. $\boldsymbol{P}_{\theta_0}\boldsymbol{H}_e\boldsymbol{P}_{\theta_0}^{-1}$ transforms $\boldsymbol{H}_e$, which is a transfer matrix in stationary frame, to $\boldsymbol{H}_{edq}$ in the grid *dq* frame. $\boldsymbol{H}_{edq}$ can be obtained by the frequency mapping technique [33]. However, for the sake of order reduction, it can

$$\begin{bmatrix}e_{d\mathrm{err}}\\ e_{q\mathrm{err}}\end{bmatrix} = \begin{bmatrix}-\frac{f_l}{f_+}E_+\sin(\omega_+ t+\delta_{e+})\sin(\theta_0)+\frac{f_l}{f_-}E_-\sin(\omega_- t+\delta_{e-})\sin(\theta_0)\\ -\frac{f_l}{f_+}E_+\sin(\omega_+ t+\delta_{e+})\cos(\theta_0)+\frac{f_l}{f_-}E_-\sin(\omega_- t+\delta_{e-})\cos(\theta_0)\end{bmatrix} \qquad (12)$$

be simplified as

$$\boldsymbol{H}_{edq} = \begin{bmatrix} H_{edq} & 0 \\ 0 & H_{edq} \end{bmatrix} \qquad H_{edq} = \frac{1}{(1/K_{e\mathrm{SOGI}})(1/\omega_0 + T_0/8)s+1} \tag{20}$$

without considering the small off-diagonal elements [7]. From (18)–(20), we can get

$$\Delta e_d^c = H_{edq}\Delta e_d + H_{edq}T_{(1,2)}\Delta e_q \tag{21}$$

$$\Delta e_q^c = -H_{edq}e_{d0}\Delta\theta + H_{edq}\Delta e_q + H_{edq}T_{(2,1)}\Delta e_d \tag{22}$$

when the initial phase δ_{e0} of the steady-state voltage variable $e_{\alpha 0}$ is set to 0, which means e_{q0} is 0. The subscript (*m*,*n*) of letter *T* denotes the *m*th row and *n*th column element of matrix ***T***.

The dynamic of PLL gives

$$\Delta\omega = s\Delta\theta = \left(Kp_{pll} + \frac{Ki_{pll}}{s}\right)\Delta e_q^c = F_{pll}\Delta e_q^c \tag{23}$$

So combining (22) and (23), $\Delta\theta$ can be calculated as

$$\Delta\theta = \underbrace{\frac{F_{pll}H_{edq}T_{(2,1)}}{s + e_{d0}F_{pll}H_{edq}}}_{G_{dpll}}\Delta e_d + \underbrace{\frac{F_{pll}H_{edq}}{s + E_{d0}F_{pll}H_{edq}}}_{G_{qpll}}\Delta e_q \tag{24}$$

From (21), (22), and (24), it follows that

$$\Delta\boldsymbol{e}^c = \underbrace{\begin{bmatrix} H_{edq} & H_{edq}T_{(1,2)} \\ H_{edq}T_{(2,1)} - H_{edq}e_{d0}G_{dpll} & H_{edq} - H_{edq}e_{d0}G_{qpll} \end{bmatrix}}_{\boldsymbol{G}_{epll}}\Delta\boldsymbol{e} \tag{25}$$

2) Current Synchronization System: The CSS has the same structure as the VSS, except that the CSS has no PLL. The LSC current vector $\boldsymbol{i}^c$ in the controller *dq* frame can be expressed as [cf., (18)]

$$\boldsymbol{i}^c \approx \boldsymbol{P}_{\Delta\theta}\boldsymbol{H}_{idq}(\boldsymbol{i}_0 + \boldsymbol{T}\Delta\boldsymbol{i}). \tag{26}$$

Since the SOGI of CSS may use a different parameter $K_{i\mathrm{SOGI}}$, the diagonal element of $\boldsymbol{H}_{idq}$ will be [cf.,(20)]

$$H_{idq} = \frac{1}{(1/K_{i\mathrm{SOGI}})(1/\omega_0 + T_0/8)s + 1} \tag{27}$$

From (24), (26), and (27), we get

$$\Delta\boldsymbol{i}^c = \underbrace{\begin{bmatrix} H_{idq} & H_{idq}T_{(1,2)} \\ H_{idq}T_{(2,1)} & H_{idq} \end{bmatrix}}_{\boldsymbol{H}_{\mathrm{SOGI}}}\Delta\boldsymbol{i} - \underbrace{\begin{bmatrix} -i_{q0}H_{idq}G_{dpll} & -i_{q0}H_{idq}G_{qpll} \\ i_{d0}H_{idq}G_{dpll} & i_{d0}H_{idq}G_{qpll} \end{bmatrix}}_{\boldsymbol{G}_{ipll}}\Delta\boldsymbol{e} \tag{28}$$

C. AC Current Loop

Applying KVL on the LSC ac loop in Fig. 4, we get

$$e_\alpha = v_\alpha + L_{\mathrm{in}}\frac{di_\alpha}{dt} + R_{\mathrm{in}}i_\alpha \tag{29}$$

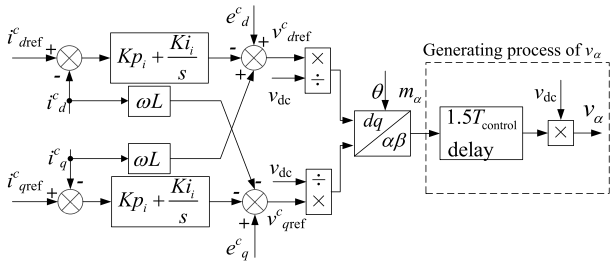

Fig. 6. Structure of ac current controller.

The frequency-domain expression of (29) in the grid *dq* frame can be obtained by the proposed *dq* decomposition of the single-phase ac variables e_α, i_α, and v_α [cf., (4)]

$$\boldsymbol{e} = \boldsymbol{v} + \underbrace{\begin{bmatrix} \frac{1}{sL_{\mathrm{in}} + R_{\mathrm{in}}} & 0 \\ 0 & \frac{1}{sL_{\mathrm{in}} + R_{\mathrm{in}}} \end{bmatrix}^{-1}}_{\boldsymbol{H}_{RL}^{-1}}\boldsymbol{i} + \underbrace{\begin{bmatrix} 0 & -\omega_0 L_{\mathrm{in}} \\ \omega_0 L_{\mathrm{in}} & 0 \end{bmatrix}}_{\boldsymbol{H}_{\omega L}}\boldsymbol{i}$$

$$\text{i.e.,}\ \boldsymbol{i} = (\boldsymbol{H}_{RL}^{-1} + \boldsymbol{H}_{\omega L})^{-1}(\boldsymbol{e} - \boldsymbol{v}) \tag{30}$$

From (30) and Fig. 4, it is obvious that the ACC uses the output of DVC $\boldsymbol{i}^c_{\mathrm{ref}}$ as the reference input and generates the reference signal $\boldsymbol{v}^c_{\mathrm{ref}}$ of $\boldsymbol{v}$ to control the LSC current $\boldsymbol{i}$. But unlike $\Delta\boldsymbol{e}$ to $\Delta\boldsymbol{e}^c$ and $\Delta\boldsymbol{i}$ to $\Delta\boldsymbol{i}^c$, there is no synchronization system to transform $\Delta\boldsymbol{v}$ to $\Delta\boldsymbol{v}^c_{\mathrm{ref}}$. So their relationship should be calculated by the generating process of v_α, which is shown in Fig. 6.

In Fig. 6, m_α is the PWM modulation signal and the $1.5T_{\mathrm{control}}$ delay is due to the computation delay and the PWM delay effect [34]. Since $\boldsymbol{v}^c_{\mathrm{ref}}$ is divided by v_{dc} inside the controller and then multiplied by v_{dc} in the generation process of v_α, the influence of v_{dc} dynamics on $\Delta\boldsymbol{v}^c_{\mathrm{ref}}$ to $\Delta\boldsymbol{v}$ will be cancelled. With the above discussion and according to Fig. 6, $\boldsymbol{v}^c_{\mathrm{ref}}$ is actually transformed to the stationary-frame variable v^c_α at first and, then, delayed by $1.5T_{\mathrm{control}}$ to obtain v_α. As the synchronous angle of the inverse Park transformation in ACC is θ, v^c_α can be calculated as

$$v^c_\alpha = v^c_{d\mathrm{ref}}\cos\theta - v^c_{q\mathrm{ref}}\sin\theta \tag{31}$$

v^c_α can also be expressed in the grid *dq* frame with the synchronous angle θ_0 as

$$v^c_\alpha = v_{d\mathrm{ref}}\cos\theta_0 - v_{q\mathrm{ref}}\sin\theta_0 \tag{32}$$

Then, from (19), (24), (31), and (32), the corresponding grid *dq*-frame expression $\Delta\boldsymbol{v}_{\mathrm{ref}} = [\Delta v_{d\mathrm{ref}}\ \Delta v_{q\mathrm{ref}}]^T$ of Δv^c_α can be derived as

$$\Delta\boldsymbol{v}_{\mathrm{ref}} = \Delta\boldsymbol{v}^c_{\mathrm{ref}} + \underbrace{\begin{bmatrix} -v^c_{q\mathrm{ref}0}G_{dpll} & -v^c_{q\mathrm{ref}0}G_{qpll} \\ v^c_{d\mathrm{ref}0}G_{dpll} & v^c_{d\mathrm{ref}0}G_{qpll} \end{bmatrix}}_{\boldsymbol{G}_{vpll}}\Delta\boldsymbol{e} \tag{33}$$

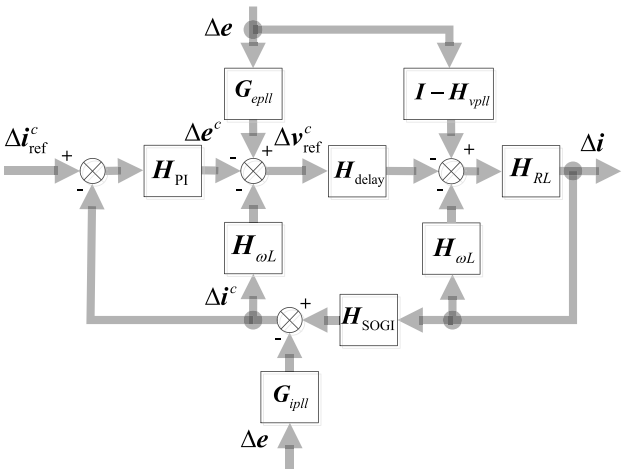

Fig. 7. Control block diagram of ac current loop.

As for the delay effect on v_α^c, it can be expressed with the assumption that a small-signal variation only consists of stable f_+ and f_- components, as

$$\Delta v_\alpha^c = V_+^c \cos(\omega_+ t + \delta_{v+}^c) + V_-^c \cos(\omega_- t + \delta_{v-}^c) \tag{34}$$

Let $T_d = 1.5T_{\text{control}}$, then

$$\begin{aligned}\Delta v_\alpha = \; & V_+^c \cos[\omega_+(t - T_d) + \delta_{v+}^c] \\ & + V_-^c \cos[\omega_-(t - T_d) + \delta_{v-}^c]\end{aligned} \tag{35}$$

Compare the grid *dq* frame expression of Δv_α^c and Δv_α obtained by (2) and (3), we get

$$\begin{aligned}\Delta \boldsymbol{v} = & \begin{bmatrix} 1 & \omega_0 T_d \\ -\omega_0 T_d & 1 \end{bmatrix} \Delta \boldsymbol{v}_{\text{ref}} = \boldsymbol{H}_{\text{delay}} \Delta \boldsymbol{v}_{\text{ref}} \\ = \; & \boldsymbol{H}_{\text{delay}} \Delta \boldsymbol{v}_{\text{ref}}^c + \underbrace{\boldsymbol{H}_{\text{delay}} \boldsymbol{G}_{vpll}}_{\boldsymbol{H}_{vpll}} \Delta \boldsymbol{e}\end{aligned} \tag{36}$$

Therefore, the control block diagram of the ac current loop can be readily obtained. Since the *d*-axis *and q*-axis variables are analyzed together as the vector form in the above discussion, the *dq*-frame vector serves as the variable flow in the control block diagram as shown in Fig. 7. The unmentioned transfer matrices in Fig. 7 are

$$\boldsymbol{I} = \begin{bmatrix} 1 & 0 \\ 0 & 1 \end{bmatrix} \tag{37}$$

$$\boldsymbol{H}_{\text{PI}} = \begin{bmatrix} Kp_i + \frac{Ki_i}{s} & 0 \\ 0 & Kp_i + \frac{Ki_i}{s} \end{bmatrix} \tag{38}$$

It is obvious that the output $\Delta \boldsymbol{i}$ of the ac current loop is affected by its reference $\Delta \boldsymbol{i}_{\text{ref}}^c$ and the disturbance $\Delta \boldsymbol{e}$. So $\Delta \boldsymbol{i}$ can be expressed as

$$\Delta \boldsymbol{i} = \boldsymbol{G}_{icl} \Delta \boldsymbol{i}_{\text{ref}}^c + \boldsymbol{G}_{\text{edis}} \Delta \boldsymbol{e} \tag{39}$$

$\boldsymbol{G}_{icl}$ and $\boldsymbol{G}_{\text{edis}}$ can be calculated from Fig. 7 as

$$\begin{aligned}\boldsymbol{G}_{icl} = \{ & \boldsymbol{I} + \boldsymbol{H}_{RL} \boldsymbol{H}_{\text{delay}} \boldsymbol{H}_{\text{PI}} \times [(\boldsymbol{I} - \boldsymbol{H}_{\text{PI}}^{-1} \boldsymbol{H}_{\omega L}) \times \boldsymbol{H}_{\text{SOGI}} \\ & + \boldsymbol{H}_{\text{PI}}^{-1} \boldsymbol{H}_{\text{delay}}^{-1} \boldsymbol{H}_{\omega L}] \}^{-1} \times (\boldsymbol{H}_{RL} \boldsymbol{H}_{\text{delay}} \boldsymbol{H}_{\text{PI}})\end{aligned} \tag{40}$$

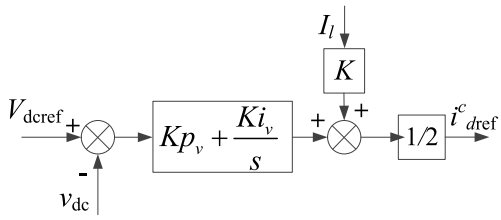

Fig. 8. Structure of DVC.

$$\begin{aligned}\boldsymbol{G}_{\text{edis}} = \; & \{\boldsymbol{I} + \boldsymbol{H}_{RL} \times [\boldsymbol{H}_{\text{delay}} (\boldsymbol{H}_{\text{PI}} - \boldsymbol{H}_{\omega L}) \boldsymbol{H}_{\text{SOGI}} \\ & + \boldsymbol{H}_{\omega L}]\}^{-1} \times \boldsymbol{H}_{RL} \times [\boldsymbol{I} - \boldsymbol{H}_{vpll} - \boldsymbol{H}_{\text{delay}} \boldsymbol{G}_{epll} \\ & + \boldsymbol{H}_{\text{delay}} (\boldsymbol{H}_{\text{PI}} - \boldsymbol{H}_{\omega L}) \boldsymbol{G}_{ipll}]\end{aligned} \tag{41}$$

D. DC Voltage Loop

The dc voltage loop is constructed by applying KCL on node D in Fig. 4. The node equation can be transformed into the frequency domain as

$$i_{\text{dc}} = \frac{sCR + 1}{R} v_{\text{dc}} + I_l \tag{42}$$

The DVC generates the reference $i_{d\text{ref}}^c$ of i_d, which represents the active power, as shown in Fig. 8.

The feed-forward signal I_l is applied in order to decrease the effect of large load variations, otherwise Kp_v would be large and cause instability [28]. *K* is a preset transfer coefficient of I_l to i_d, which is obtained by the power balance principle. $i_{d\text{ref}}^c$ is reduced to half since it is just the current reference of one paralleled LSC. The relation between Δi_d and Δi_{dc} can be obtained by the instantaneous power balance between the ac side and the dc side of one converter bridge, which can be expressed as

$$(v_d \cos\theta_0 - v_q \sin\theta_0)(i_d \cos\theta_0 - i_q \sin\theta_0) = v_{\text{dc}} i_{\text{dc}} \tag{43}$$

As CRH_5 is in the light-load condition when the LFO happens, the second-order harmonic component is small and, then, can be neglected. So (43) can be simplified as

$$\frac{1}{2}(v_d i_d + v_q i_q) = v_{\text{dc}} i_{\text{dc}} \tag{44}$$

Equation (44) can be linearized around the steady-state operation point as

$$\begin{aligned}\frac{1}{2}(v_{d0} \Delta i_d + i_{d0} \Delta v_d + v_{q0} \Delta i_q + i_{q0} \Delta v_q) \\ = v_{\text{dc}0} \Delta i_{\text{dc}} + i_{\text{dc}0} \Delta v_{\text{dc}}.\end{aligned} \tag{45}$$

The variables i_{d0}, v_{q0}, i_{q0}, and $i_{\text{dc}0}$ are all of small values in the light-load condition and will be omitted to reach a more simple and explicit equation

$$\Delta i_{\text{dc}} = \frac{v_{d0}}{2 v_{\text{dc}0}} \Delta i_d = K' \Delta i_d \tag{46}$$

where K' is close to *K* but has a slight shift due to the change of LSC steady-state operation point. Then, the dc voltage loop is readily obtained with the above discussion and shown in Fig. 9. Because V_{dcref} and I_l are constant, they are not included in

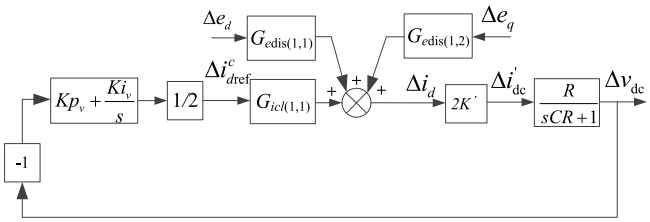

Fig. 9. Control block diagram of dc voltage loop.

the dc voltage loop. $\Delta i'_{\mathrm{dc}}$ equals to $2\Delta i_{\mathrm{dc}}$ because the dc-link assembles two paralleled LSCs' currents.

From Fig. 9, we can find that $\Delta i^c_{d\mathrm{ref}}$ is only affected by $\Delta \boldsymbol{e}$ and their relation can be expressed as

$$\Delta i^c_{d\mathrm{ref}} = \begin{bmatrix} G'_{e\mathrm{dis}(1,1)} & G'_{e\mathrm{dis}(1,2)} \end{bmatrix} \Delta \boldsymbol{e} \tag{47}$$

where

$$G'_{e\mathrm{dis}(1,1)} = \frac{-\frac{1}{2}\frac{R}{sCR+1}(Kp_v + \frac{Ki_v}{s})K'G_{e\mathrm{dis}(1,1)}}{1+\frac{1}{2}\frac{R}{sCR+1}\left(Kp_v+\frac{Ki_v}{s}\right)K'G_{icl(1,1)}}$$

$$G'_{e\mathrm{dis}(1,2)} = \frac{-\frac{1}{2}\frac{R}{sCR+1}\left(Kp_v + \frac{Ki_v}{s}\right)K'G_{e\mathrm{dis}(1,2)}}{1+\frac{1}{2}\frac{R}{sCR+1}\left(Kp_v+\frac{Ki_v}{s}\right)K'G_{icl(1,1)}} \tag{48}$$

Considering that $i^c_{q\mathrm{ref}}$ is a preset value and will not change in the light-load condition (i.e., $\Delta i^c_{q\mathrm{ref}}$ is 0), $\Delta \boldsymbol{i}^c_{\mathrm{ref}}$ can be expressed as

$$\Delta \boldsymbol{i}^c_{\mathrm{ref}} = \begin{bmatrix} G'_{e\mathrm{dis}(1,1)} & G'_{e\mathrm{dis}(1,2)} \\ 0 & 0 \end{bmatrix} \Delta \boldsymbol{e} = \boldsymbol{G}'_{e\mathrm{dis}} \Delta \boldsymbol{e} \tag{49}$$

E. Input Admittance Matrix and Its Verification

From (39) and (49), the expression of the LSC current variation $\Delta \boldsymbol{i}$ caused by the small input voltage disturbance $\Delta \boldsymbol{e}$ around a certain operating point can be calculated as

$$\Delta \boldsymbol{i} = (\boldsymbol{G}_{icl}\boldsymbol{G}'_{e\mathrm{dis}} + \boldsymbol{G}_{e\mathrm{dis}})\Delta \boldsymbol{e} = \underbrace{\begin{bmatrix} Y_{dd} & Y_{dq} \\ Y_{qd} & Y_{qq} \end{bmatrix}}_{\boldsymbol{Y}} \Delta \boldsymbol{e} \tag{50}$$

where $\boldsymbol{Y}$ is the input admittance matrix of one LSC and will be verified by the previously mentioned low-frequency sweep experiment.

At the very beginning of the verification experiment, the simulated LSC will be operating in a steady state with a light-load current I_l and an ideal voltage source e_{s0} added in terminal AB of Fig. 4. Then, a *dq*-frame sinusoidal disturbance Δe_d at a low-frequency f_l will be transformed to a single-phase ac signal Δe_α according to (2) and will be added to e_{s0}. After the LSC reaches the steady state, Δi_d and Δi_q can be calculated by the *dq* decomposition of Δi_α, which is measurable. By repeating the experiment with different frequencies (1–15 Hz) for Δe_d, we can acquire the magnitude and phase responses of Y_{dd} and Y_{qd} in the concerned frequency range from (6). The same procedure will be taken with the disturbance signal Δe_q to obtain the magnitude and phase responses of Y_{dq} and Y_{qq}. The simulated and the model-predicted frequency response of the input admittance matrix are compared in Fig. 10. It is obvious that the model-predicted values agree with the simulated values well except for $|Y_{dq}|$ and $|Y_{qd}|$ in relative high frequencies. The inconformity of the mutual admittance magnitudes comes from the simplification processes in (12) and (20), which decrease the model order and hence the risk of singular matrix. However, it brings little impact on the following vehicle-grid system analysis especially in the low-frequency range.

IV. Model of Vehicle-Grid System

Since the traction power feeding grid is considered as a linear circuit as previously discussed, its small-signal model $\boldsymbol{Z}_s$ in grid *dq* frame can be easily acquired. Then, the vehicle-grid system model can be obtained by connecting the *m* vehicles (LSCs) subsystem model and the grid subsystem model together after calculating the steady-state operation point of the entire system.

A. Steady-State Operation Point of Vehicle-Grid System

First, the steady-state PCC voltage should be solved with the known total load current and no-load source voltage by the traditional power flow calculation. But in *dq* frame, it should be solved by the *dq* decomposition of (51) that is obtained by applying KVL on the left part of PCC in Fig. 2

$$e_{s0} = e_0 + L_s\frac{di_{\mathrm{sum}0}}{dt} + R_s i_{\mathrm{sum}0} \tag{51}$$

As the *m* vehicles are of the same type and in the same operating state, the total vehicle current can be calculated as *m* times of the single vehicle current. So in (51), $i_{\mathrm{sum}0} = (10m)i_0 = ni_0$, where *n* is the number of the equivalent LSCs. In order to make the grid *dq* frame and the controller *dq* frame rotate with the same initial angle and speed in the steady state, which is a necessary assumption during the modeling, the initial phase of e_0 is forced to be 0 and will serve as the reference for any steady state of the vehicle-gird system. As a result, the initial phase δ_{es0} of the constant voltage source e_{s0} will change relatively to the setting reference with different steady states. With the discussion above, the steady-state operation point can be calculated as

$$\begin{aligned} \delta_{es0} &= \arcsin\frac{n\omega_0 L_s I_l/K + nR_s i^c_{q\mathrm{ref}}}{E_{s0}} \\ e_{d0} &= E_{s0}\cos\delta_{es0} + n\omega_0 L_s i^c_{q\mathrm{ref}} - nR_s I_l/K \end{aligned} \tag{52}$$

where E_{s0} denotes the amplitude of e_{s0}.

Second, the steady-state ac-side voltage of the converter bridge can be obtained by the *dq* composition of the steady-state form of (29) and be expressed as

$$\begin{aligned} v_{d0} &= e_{d0} + \omega_0 L_{\mathrm{in}} i^c_{q\mathrm{ref}} - R_{\mathrm{in}} I_l/K \\ v_{q0} &= -\omega_0 L_{\mathrm{in}} I_l/K - R_{\mathrm{in}} i^c_{q\mathrm{ref}}. \end{aligned} \tag{53}$$

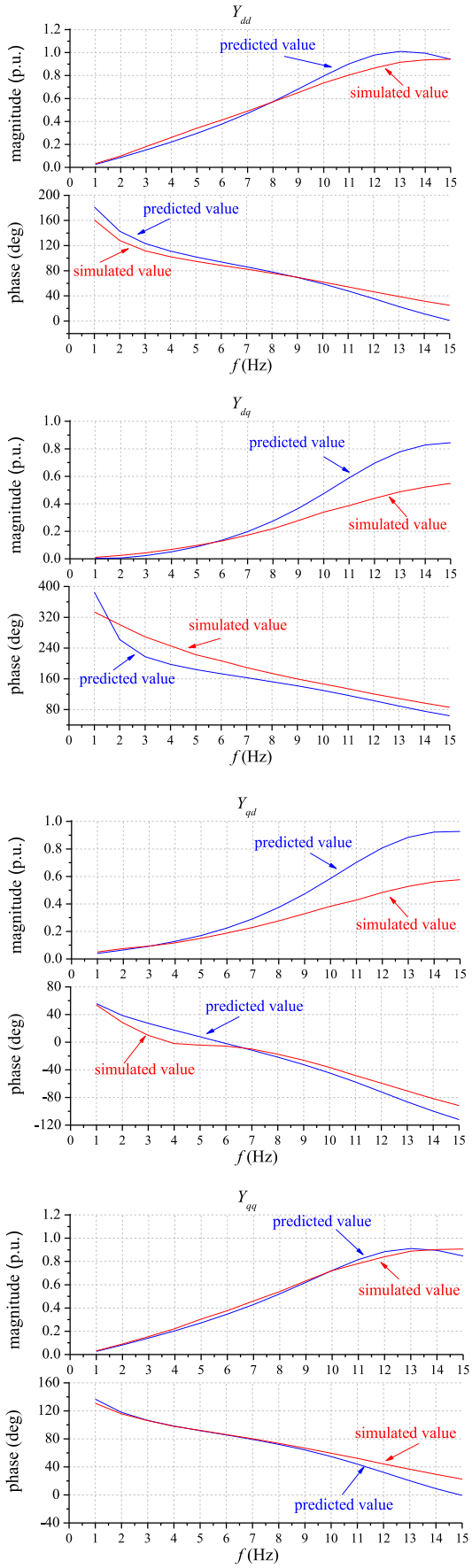

Fig. 10. Simulated and predicted frequency response of $\boldsymbol{Y}$.

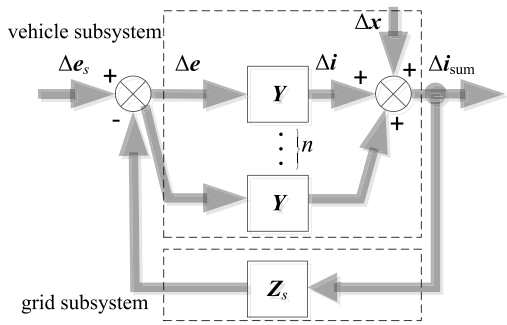

Fig. 11. Closed-loop structure of vehicle-grid system.

Additionally in the dc side of the converter bridge, the steady-state dc-link voltage v_{dc0} is set as V_{dcref}. The related parameters and values in (52) and (53) are given in Appendix.

B. Small-Signal Model of Vehicle-Grid System

The small-signal expression of (51) is

$$\Delta e_s = \Delta e + nL_s \frac{d\Delta i}{dt} + nR_s \Delta i \tag{54}$$

It can also be decomposed in the grid dq frame as [cf., (30)]

$$\Delta \boldsymbol{e}_s = \Delta \boldsymbol{e} + \underbrace{\begin{bmatrix} sL_s + R_s & -\omega_0 L_s \\ \omega_0 L_s & sL_s + R_s \end{bmatrix}}_{\boldsymbol{Z}_s} n\Delta \boldsymbol{i} \tag{55}$$

If we treat the total line current $\Delta \boldsymbol{i}_{\text{sum}} = n\Delta \boldsymbol{i}$ as output and $\Delta \boldsymbol{e}_s$ as input, the vehicle-grid system can be readily built from (50) and (55) as a closed-loop system as shown in Fig. 11.

The closed-loop transfer matrix can be obtained from Fig. 11 as

$$\Delta \boldsymbol{i}_{\text{sum}} = \frac{n\boldsymbol{Y}}{\boldsymbol{I} + \underbrace{n\boldsymbol{Y}}_{\boldsymbol{Y}_{\text{sum}}} \boldsymbol{Z}_s} \Delta \boldsymbol{e}_s = \boldsymbol{H}_{cl} \Delta \boldsymbol{e}_s \tag{56}$$

The small-signal model of the vehicle-grid system can then be derived. Besides, $\Delta \boldsymbol{x}$ in Fig. 11 represents some predictable disturbances and will be further explained in the next section.

V. Stability Analysis of Vehicle-Grid System

In order to determine whether the vehicle-grid system in Fig. 11 is stable, the stability analysis theory of a MIMO system should be applied.

A. MIMO System Stability Criterion

The zeros and poles of a square transfer matrix $\boldsymbol{G}$ are defined as the roots of the numerator polynomials $z(s)$ and denominator polynomials $p(s)$, which are obtained by

$$\frac{z(s)}{p(s)} = \det(\boldsymbol{G}) \tag{57}$$

where $\boldsymbol{G}$ is stable if and only if it has no positive poles. Then, a feedback system depicted in Fig. 12 is stable if the following conditions are satisfied [35].

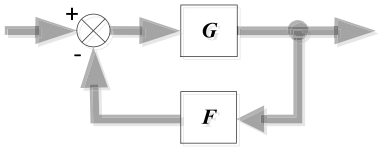

Fig. 12. General MIMO feedback system.

TABLE II
DOMINANT POLES IN DIFFERENT SYSTEM CONDITIONS
(10-KM CONTACT LINE)

No.	LSC number and load current	Dominant poles (1/s) $\pm j$(Hz)	Damping factor	Simulation result
1	$n = 50$, $I_l = 0.0075$	$-0.28 \pm j5.73$	0.050	stable
2	$n = 60$, $I_l = 0.0075$	$-0.03 \pm j5.22$	0.006	critically stable
3	$n = 60$, $I_l = 0.015$	$-0.04 \pm j5.22$	0.009	stable
4	$n = 70$, $I_l = 0.0075$	$0.16 \pm j4.81$	-0.034	unstable
5	$n = 70$, $I_l = 0.11$	$-0.12 \pm j4.87$	0.025	stable

1) $\boldsymbol{F}$ is stable.
2) The open-loop transfer matrix $\boldsymbol{G}_{ol} = \boldsymbol{I} + \boldsymbol{GF}$ has no positive zeros.
3) The closed-loop transfer matrix $\boldsymbol{H}_{cl} = (\boldsymbol{I} + \boldsymbol{GF})^{-1}\boldsymbol{G}$ is analytic (i.e., has no poles) at all positive poles of $\boldsymbol{G}$.

B. Underdamped Mechanism of LFO in Electric Railway

As for the vehicle-grid system, the feedback transfer matrix $\boldsymbol{Z}_s$ is naturally stable. Additionally, the forward-path transfer matrix $\boldsymbol{Y}_{\text{sum}}$ will also be stable with controller parameters setting in a reasonable range. The only risk that may cause instability is the possible positive zeros in the open-loop transfer matrix $\boldsymbol{G}_{ol} = \boldsymbol{I} + \boldsymbol{Y}_{\text{sum}}\boldsymbol{Z}_s$. After a carefully observation of the zeros of $\boldsymbol{G}_{ol}$, it can be readily found that one special pair of conjugate zeros, whose damping oscillation frequency just corresponds to the LFO frequency, are always the nearest to the imaginary axis and noted as r_1 and r_2. Since the zeros of $\boldsymbol{G}_{ol}$ will exist in poles of $\boldsymbol{H}_{cl}$, r_1 and r_2 can be regarded as the dominant poles of the vehicle-grid system as defined in a SISO linear system.

To verify the important role of the dominant poles, the system condition is adjusted till the LFO occurs in a vehicle-grid simulation. The stable oscillation, which is very similar to Fig. 1, happens when the system is under No. 2 system condition of Table II and is shown in Fig. 13. The dominant poles under this condition are $-0.03 \pm j5.22$, which demonstrate a possible 5.22-Hz oscillation frequency and a small but positive damping factor 0.006. Therefore, the simulated stable oscillation at 5.03 Hz is well predicted by the dominant poles with an adequate accuracy. This stable oscillation state can also be called as the critically stable state because the damping factor is close to 0 and this stable state can be easily damaged by small disturbances. Besides, the other two possible system states denoted as stable and unstable are also recorded in Table II, including their corresponding system conditions and dominant poles.

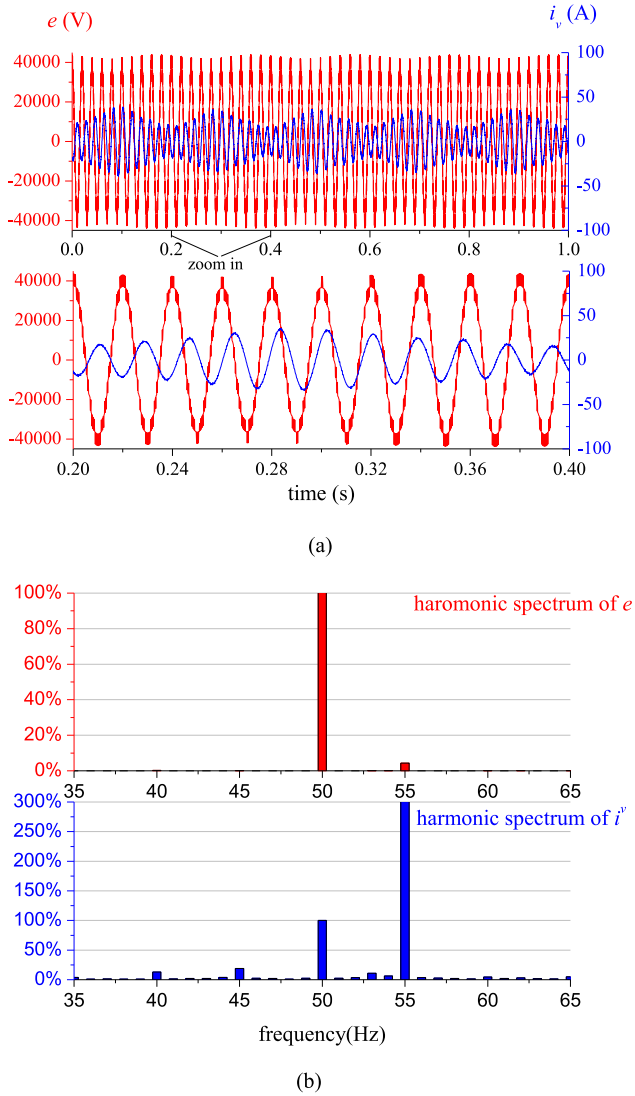

Fig. 13. (a) Simulated oscillation waveforms. (b) Harmonic spectrum of simulated oscillation waveforms.

In the linear control theory, the output of a system can just have the frequency components that the input source has unless the system is critical damping at a specific frequency. Although there does not exist such a low-frequency source in the vehicle-grid system, a lot of lasting disturbance sources, such as a source voltage fluctuation $\Delta \boldsymbol{e}_s$ and a current disturbance $\Delta \boldsymbol{x}$ generated by the change of LSC load current ΔI_l or a sudden start-up of a vehicle, will still act as the excitations and may be able to induce an oscillation in a seriously underdamped (close to critical damping as No. 2 in Table II) vehicle-grid system. In the vehicle-grid simulation, $\Delta \boldsymbol{e}_s$ and ΔI_l are set to 0, but the jump voltage generated by PWM will still cause a disturbance in the LSC current, which can behave as a periodic excitation $\Delta \boldsymbol{x}$ to the system as well. In addition, the nonlinearity of LSC and its controller can also be viewed as other lasting excitations [36]. The LFO can hence maintain with the following two conditions

being satisfied: lasting excitations and a seriously underdamped system.

C. Factors That Affect Low-Frequency Stability

Using the underdamped mechanism, one can determine whether there is a risk of LFO under a specific system condition before multiple vehicles are planned to be put into service in an electric railway. Besides, the LFO can be somewhat alleviated by modifying the controller parameters since they have close relations to the vehicles' low-frequency dynamics. The dominant-pole plots will be applied here to reveal these laws in Fig. 14. The first plot is focused on the vehicle-grid system condition, so the LSC controller parameters keep unchanged as given in Appendix. In the meanwhile, the latter three plots are designed to explore the impact of LSC controller parameters on the system stability, so the No. 2 system condition in Table II is applied and will not change.

1) Number of Vehicles and Load Current of LSC: It already can be concluded from Table II that more vehicles and lighter load will make the system more unstable.

2) Contact Line Distance: The impact of the contact line distance will be explored under the No. 2 system condition in Table II. It is readily to conclude from Fig. 14(a) that longer contact line, which in fact means a larger source impedance, will more likely cause the instability. Additionally, the potential oscillation frequency is also changed corresponding to the length of contact line. The stability of the system can be judged by the vehicle-grid simulation results and then be noted by different marks in Fig. 14.

3) SOGI Parameters: It is found that a minor change in SOGI parameters of the VSS and the CSS could alter the vehicle-grid system stability, which means that they are the most "sensitive" controller parameters [37]. It is shown in Fig. 14(b) that the system will become more stable as $K_{e_{\mathrm{SOGI}}}$ and $K_{i_{\mathrm{SOGI}}}$ arise and otherwise takes a risk of low-frequency instability.

4) ACC Parameters: The PI controller parameters in the ACC can also significantly affect the low-frequency dynamic of the LSC so that the change of them, especially Kp_i, will consequently influence the vehicle-grid system stability. Both the increase of Ki_i and the decrease of Kp_i will jeopardize the system low-frequency stability through carefully observation of Fig. 14(c).

5) DVC Parameters: The impact of the proportional coefficient Kp_v of the DVC PI controller on the vehicle-grid system stability is as remarkable as the SOGI parameters and ACC parameter Kp_i. While the impact of the integral coefficient Ki_v is not that significant. As shown in Fig. 14(d), decreasing Kp_v can effectively damp the LFO, but adjusting Ki_v cannot achieve the same effect since its value is already very small.

VI. Conclusion

The *dq*-frame components of a single-phase ac signal are defined by analyzing the LFO waveforms. With this definition, an analytical small-signal frequency-domain model of the LSC in *dq* frame has been established for the first time after carefully dealing with the main modeling obstacle. The verification

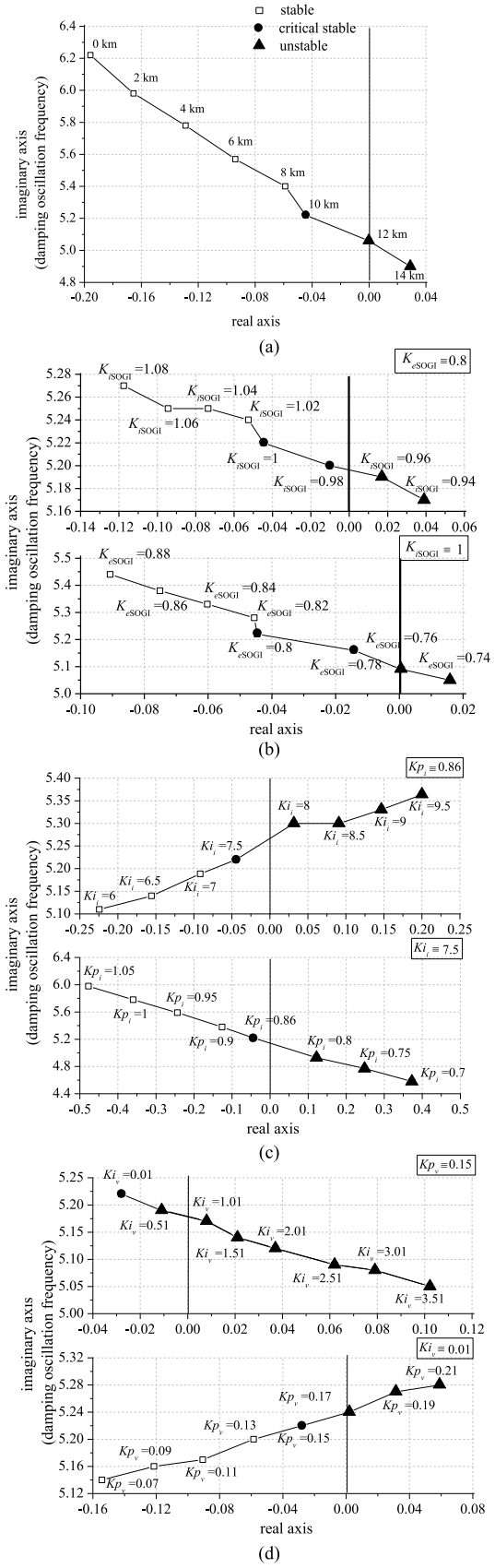

Fig. 14. Dominant-pole plots. (a) Contact-line distance. (b) SOGI Parameters. (c) ACC parameters. (d) DVC parameters.

TABLE III
BASE VALUES OF PER UNIT SYSTEM

$S_b = 2$ MVA	$V_b = V_{\mathrm{d}c}b = 2503$ V
$I_b = 1598$ A	$Z_b = 1.567\ \Omega$
$I_{\mathrm{d}c}b = 799$ A	$Z_{\mathrm{d}c}b = 3.133\ \Omega$

TABLE IV
LSC CIRCUIT PARAMETERS AND ITS CONTROLLER PARAMETERS

$L_{\mathrm{in}} = 1.083$	$R_{\mathrm{in}} = 0.0932$
$C = 0.1129$	$R = 4788$
$V_{\mathrm{d}c} = 1.278$	$I_l = 0.0075$
$Kp_{pll} = 51$	$Ki_{pll} = 64.56$
$K_{\mathrm{eSOGI}} = 0.8$	$K_{\mathrm{iSOGI}} = 1$
$Kp_i = 0.86$	$Ki_i = 7.5$
$Kp_v = 0.15$	$Ki_v = 0.01$
$K = 0.7822$	$T_{\mathrm{control}} = 0.0001$

TABLE V
TRACTION POWER SUPPLY SYSTEM PARAMETERS

$E_{s0} = 1.1$	$L_c = 0.0009$
$L_s = 0.0338$	$R_s = 0.0037$

experiment not only proves the validity and accuracy of the proposed model but also provides a way to obtain the numerical LSC model without knowing its inner control design.

Since the vehicle is represented by multiple LSCs and the grid is considered as a Thevinen equivalent circuit, the vehicle-grid system can be modeled as a close-loop transfer matrix, whose stability can be analyzed by the linear MIMO system theory. Based on this model, the under-damped mechanism is proposed to explain the LFO phenomenon through studying the system dominant poles and finding out the lasting excitations for the oscillation.

The dominant-pole plot is a convenient and quick tool to predict the vehicle-grid system stability under the different system conditions and the LSC controller parameters. So this method will be suitable for prejudge the LFO and therefore help decide the train dispatching plan. Besides, when the instability happens, it can become a useful guidance of how to damp the LFO problem by modifying the LSC controller parameters.

Although only CRH_5 LSC is modeled in this paper, it should be pointed out that this modeling method can be considered as a generous method for modeling different types of vehicle LSCs. The future study will be focused on applying this method more widely and proposing the countermeasures for damping the LFO in different vehicle cases.

APPENDIX

The parameters used in this paper will be listed in the following tables. Some specifications are listed: 1) The values in Table III refer to the rated values in the traction-winding side of CRH_5 traction transformer. 2) The DVC PI controller parameters in Table IV are small since they are just set for LSC start and standstill operation states. 3) L_c in Table V is the inductance of contact line per kilometer.

REFERENCES

[1] C. Heising, J. Fang, R. Bartelt, V. Staudt, and A. Steimel, "Modelling of rotary converter in electrical railway traction power-systems for stability analysis," in *Proc. Electr. Syst. Aircraft, Railway Ship Propul.*, 2010, pp. 1–6.

[2] M. Wu and H. Wang, "The test of traction power blocking of CRH_5 EMU caused by the voltage oscillation," Beijing Jiaotong Univ., Beijing, China, Tech. Rep. E11L00040, Sep. 26, 2010.

[3] Q. Zheng, "A probe on causes and solutions of HXD1 AC locomotive's resonance," *World Inverters*, vol. 5, pp. 40–44, 2009.

[4] Q. Li, "Electric matching problems in traction power supply system," *Electr. Railway*, vol. 3, pp. 13–16, 2014.

[5] C. Heising, R. Bartelt, M. Oettmeier, V. Staudt, and A. Steimel, "Enhancement of low-frequency system stability of 60-Hz railway power grids," in *Proc. Power Electron. Motion Control Conf.*, 2010, pp. S7–1–S7-8.

[6] S. Danielsen, M. Molinas, T. Toftevaag, and O. B. Fosso, "Constant power load characteristic's influence on the low-frequency interaction between advanced electrical rail vehicle and railway traction power supply with rotary converters," in *Proc. Modern Electr. Traction*, 2009, pp. 1–6.

[7] S. Danielsen, O. B. Fosso, M. Molinas, J. A. Suul, and T. Toftevaag, "Simplified models of a single-phase power electronic inverter for railway power system stability analysis—Development and evaluation," *Electr. Power Syst. Res.*, vol. 80, no. 2, pp. 204–214, Feb. 2010.

[8] C. Heising, M. Oettmeier, V. Staudt, A. Steimel, and S. Danielsen, "Improvement of low-frequency railway power system stability using an advanced multivariable control concept," in *Proc. IEEE 35th Annu. Conf. Ind. Electron.*, 2009, pp. 560–565.

[9] J. M. Alonso, D. Gacio, F. Sichirollo, A. R. Seidel, and M. A. Dalla Costa, "A straightforward methodology to modeling high power factor AC–DC converters," *IEEE Trans. Power Electron.*, vol. 28, no. 10, pp. 4723–4731, Oct. 2013.

[10] S. Vesti, T. Suntio, J. A. Oliver, R. Prieto, and J. A. Cobos, "Effect of control method on impedance-based interactions in a buck converter," *IEEE Trans. Power Electron.*, vol. 28, no. 11, pp. 5311–5322, Nov. 2013.

[11] C. Byungcho, K. Dongsoo, L. Donggyu, C. Seungwon, and S. Jian, "Analysis of input filter interactions in switching power converters," *IEEE Trans. Power Electron.*, vol. 22, no. 2, pp. 452–460, Mar. 2007.

[12] L. Harnefors, M. Bongiorno, and S. Lundberg, "Input-admittance calculation and shaping for controlled voltage-source converters" *IEEE Trans. Power Del.*, vol. 54, no. 6, pp. 3323–3334, Dec. 2007.

[13] L. Harnefors, "Analysis of subsynchronous torsional interaction with power electronic converters," *IEEE Trans. Power Syst.*, vol. 22, no. 1, pp. 305–313, Dec. 2007.

[14] X. Wang, F. Blaabjerg, and W. Wu, "Modeling and analysis of harmonic stability in an AC power-electronics-based power system," *IEEE Trans. Power Electron.*, vol. 29, no. 12, pp. 6421–6432, Dec. 2014.

[15] B. Wen, D. Boroyevich, P. Mattavelli, Z. Shen, and R. Burgos, "Influence of phase-locked loop on input admittance of three-phase voltage-source converters," in *Proc. Appl. Power Electron. Conf. Expo.*, 2013, pp. 897–904.

[16] J. Sun, "Impedance-based stability criterion for grid-connected inverters," *IEEE Trans. Power Electron.*, vol. 26, no. 11, pp. 3075–3078, Nov. 2011.

[17] J. Sun, "Small-signal methods for AC distributed power systems—A review," *IEEE Trans. Power Electron.*, vol. 24, no. 11, pp. 2545–2554, Nov. 2009.

[18] M. Chen and J. Sun, "Low-frequency input impedance modeling of boost single-phase PFC converters," *IEEE Trans. Power Electron.*, vol. 22, no. 4, pp. 1402–1409, Jul. 2007.

[19] M. Cespedes and J. Sun, "Renewable energy systems instability involving grid-parallel inverters," in *Proc. IEEE 24th Annu. Conf. Appl. Power Electron.*, 2009, pp. 1971–1977.

[20] G. Ledwich and H. Sharma, "Connection of inverters to a weak grid," in *Proc. IEEE 31st Annu. Conf. Power Electron. Spec.*, 2000, pp. 1018–1022.

[21] J. Sun and K. J. Karimi, "Small-signal input impedance modeling of line-frequency rectifiers," *IEEE Trans. Aerosp. Electron. Syst.*, vol. 44, no. 4, pp. 1489–1497, Oct. 2008.

[22] J. Sun, B. Zhonghui, and K. J. Karimi, "Input impedance modeling of multipulse rectifiers by harmonic linearization," *IEEE Trans. Power Electron.*, vol. 24, no. 12, pp. 2812–2820, Dec. 2009.

[23] H. Wang, M. Wu, V. G. Agelidis, and K. Song, "Steady-state harmonic domain matrix-based modeling of four-quadrant EMU line converter," *J. Power Electron.*, vol. 14, no. 3, pp. 572–579, May 2014.

[24] S. Menth and M. Meyer, "Low frequency power oscillations in electric railway systems," *Elektrische Bahnen*, vol. 104, no. 4, pp. 216–221, 2006.

[25] S. Pika and S. Danielsen, "Understanding of the stability criterion for a double-feedback loop system," in *Proc. Electr. Syst. Aircraft, Railway Ship Propul.*, 2010, pp. 1–5.
[26] J. Suarez, P. Ladoux, N. Roux, H. Caron, and E. Guillame, "Measurement of locomotive input admittance to analyse low frequency instability on AC rail networks," in *Proc. Int. Symp. Power Electron., Electr. Drives, Autom. Motion*, 2014, pp. 790–795.
[27] H. Wang and M. Wu, "The measurement and analysis of the low frequency oscillation in traction power supply system caused by the EMU," in *Proc. 27th Chin. Univ. Symp. Power Electr. Syst. Autom.*, Qinhuangdao, China, 2011.
[28] C. Bajracharya,, M. Molinas, J. A. Suul, and T. M. Undeland, "Understanding of tuning techniques of converter controllers for VSC-HVDC," presented at the Nordic Workshop Power Ind. Electron., Espoo, Finland, 2008.
[29] N. Wang, W. Song, and X. Feng, "Characteristics analysis and reduction of the high order harmonics of DC-link voltage for railway traction converters," in *Proc. IEEE 7th Conf. Power Electron. Motion Control*, 2012, pp. 1926–1931.
[30] J. Salaet, S. Alepuz, and A. Gilabert, "Comparison between two methods of DQ transformation for single phase converters control. Application to a 3-level boost rectifier," in *Proc. IEEE 35th Annu. Conf. Power Electron. Spec.*, 2004, pp. 214–220.
[31] M. Karimi-Ghartemani, "A unifying approach to single-phase synchronous reference frame PLLs," *IEEE Trans. Power Electron.*, vol. 28, no. 10, pp. 4550–4556, Oct. 2013.
[32] R. Adda, O. Ray, S. K. Mishra, and A. Joshi, "Synchronous-reference-frame-based control of switched boost inverter for standalone DC nanogrid applications," *IEEE Trans. Power Electron.*, vol. 28, no. 3, pp. 1219–1233, Mar. 2013.
[33] L. Harnefors, "Modeling of three-phase dynamic systems using complex transfer functions and transfer matrices," *IEEE Trans. Ind. Electron.*, vol. 54, no. 4, pp. 2239–2248, Aug. 2007.
[34] B. H. Bae and S. K. Sul, "A compensation method for time delay of full-digital synchronous frame current regulator of PWM AC drives," *IEEE Trans. Ind. Appl.*, vol. 39, no. 3, pp. 802–810, Jun. 2003.
[35] J. M. Maciejowski, "Poles, zeros and stability of multivariable feedback systems," in *Multivariable Feedback Design*. Reading, MA, USA: Addison-Wesley, 1989, pp. 45–57.
[36] J. Sun, "Modeling and analysis of harmonic resonance involving renewable energy sources," in *Proc. Int. Conf. Power Syst. Transients*, 2013, pp. 1–7.
[37] S. Danielsen, O. B. Fosso, and T. Toftevaag, "Use of participation factors and parameter sensitivities in study and improvement of low-frequency stability between electrical rail vehicle and power supply," in *Proc. IEEE 13th Eur. Conf. Power Electron. Appl.*, 2009, pp. 1–10.

Hui Wang was born in Tianjin, China, on June 9, 1985. He received the B.Sc. degree in electrical engineering from the Huazhong University of Science and Technology, Wuhan, China. He is currently working toward the Ph.D. degree in electrical engineering at Beijing Jiaotong University, Beijing, China.

His research interests include the mechanism and the damping methods of the low-frequency oscillations in electric railways and the control strategy of line-side converters embeded on EMUs.

Wu Mingli was born in Hebei Province, China, on November 11, 1971. He received the B.Sc. and M.Sc. degrees in electrical engineering from Southwest Jiaotong University, Chengdu, China, in 1993 and 1996, respectively, and the Ph.D. degree in electrical engineering form the Beijing Jiaotong University, Beijing, China, in 2006.

Since 2008, he has been a Professor at the School of Electrical Engineering, Beijing Jiaotong University. His research interests include power supply for electric railways, digital simulation of power systems, and electric power quality.

Juanjuan Sun was born in Guiyang, China, on May 26, 1985. She received the B.Sc. degree in environmental engineering from the Huazhong University of Science and Technology, Wuhan, China, the M.Sc. degrees in environmental engineering from Peking University, Beijing, China. She is currently working toward the Ph.D. degree in mechanical engineering at the School of Mechanical, Electronic, and Control Engineering, Beijing Jiaotong University, Beijing.

Her research interest includes the optimization methodology.